Determination of spin relaxation times in heavy metals via second-harmonic spin injection magnetoresistance

C. Fang, C. H. Wan,[*] B. S. Yang, J. Y. Qin, B. S. Tao, H. Wu, X. Zhang, and X. F. Han[†]
Institute of Physics, Chinese Academy of Sciences, Beijing 100190, China
and University of Chinese Academy of Sciences, Beijing 100049, China

A. Hoffmann
Materials Science Division, Argonne National Laboratory, 9700 S. Cass Avenue, Lemont, Illinois 60439, USA

X. M. Liu and Z. M. Jin
Department of Physics, Shanghai University, Shanghai 200444, China

In tunnel junctions between ferromagnets and heavy elements with strong spin orbit coupling the magnetoresistance is usually dominated by tunneling anisotropic magnetoresistance (TAMR). This makes conventional DC spin injection techniques impractical for determining the spin relaxation time τ_s. Here, we show that this obstacle for measurements of τ_s can be overcome by second-harmonic spin-injection magnetoresistance (SIMR). In the second-harmonic signal the SIMR is comparable in magnitude to TAMR, thus enabling Hanle-induced SIMR as a powerful tool to directly determine τ_s. Using this approach we determined the spin relaxation time of Pt and Ta and their temperature dependences. The spin relaxation in Pt seems to be governed by the Elliott-Yafet mechanism due to a constant resistivity $\times$ spin relaxation time product over a wide temperature range.

I. INTRODUCTION

The remarkable applied potential of spin-orbit torques for magnetic random access memory has stimulated intensive interest in investigating spin orbit coupling (SOC) in heavy metals such as Pt and Ta [1–11]. Their spin Hall angle θ_{SH}, spin diffusion length l_s, and spin relaxation time τ_s, which influence switching efficiency, are important parameters for determining their effectiveness, but especially the latter two are experimentally hard to assess. Accurate determination of τ_s could also help to identify the spin relaxation mechanisms [12]. Though θ_{SH} and l_s have been measured by spin pumping [13–17] and second-harmonic Hall measurement [18–20], τ_s of Pt and Ta is rarely reported. In principle, $\tau_s = l_s^2/D$, with D being the diffusion constant which is also difficult to determine independently.

Electron spin resonance (ESR) has been a standard technique to measure the spin relaxation time of bulk light metals [21]. However, it is not suitable for ultrathin films [22,23]. In addition, Elezzabi *et al.* [24] developed a time-resolved optical technique to directly measure the spin relaxation process in Au to be $\tau_{s,Au} = (45 \pm 5)$ ps. However, this method is not suitable for heavy metals, such as Pt, Ta, and W, with short τ_s [25]. Recently, Dyakonov [26] theoretically, and then Vélez *et al.* [27] and Wu *et al.* [28] experimentally demonstrated a so-called Hanle magnetoresistance (MR) effect in Pt and Ta: a spin accumulation at the sample boundaries caused by the spin Hall effect is dephased by a magnetic field via the Hanle effect, which results in an additional positive MR. This electrical method can be applied to estimate τ_s from the magnetic field dependence [27,28]. Using this

approach $\tau_{s,Pt} = 1.9$ was determined for Pt/SiO$_2$ and 0.61 ps for Pt/Y$_3$Fe$_5$O$_{12}$ [28]. In fact, spin injection experiments in nonlocal spin valves [29–35] and three-terminal geometries [36–40] are both powerful tools in measuring τ_s in metals and semiconductors. In these experiments, ferromagnetic layer (FM)/tunnel barrier/nonmagnetic layer (NM) junctions are adopted to both inject a nonequilibrium spin accumulation and simultaneously determine their magnitude. These measurements were used to determine spin relaxation times in a wide variety of materials, e.g., $\tau_{s,Si} = 55$ to 285 ps for heavily doped silicon [40]; $\tau_{s,Graphene} > 1$ ns for graphene/BN [41]; $\tau_{s,Al} = 110$ ps for aluminum [29]; $\tau_{s,Cu} = 22$ ps for copper [42]; and $\tau_{s,Au} = 45$ ps for gold [32].

However, it is impractical to apply these spin injection experiments to measure τ_s in heavy metals with strong SOC for at least two reasons. First, l_s in this case is so short (about several nanometers) that the preparation of nonlocal spin valves with comparable dimensions is beyond current lithography capabilities. Second, the real contact resistance is $r = r_C + r_{SI}$, where r_{SI} and r_C are the contact resistance induced by spin injection (SI) and the original contact resistance without r_{SI}, respectively. Here r_{SI} equals to $[r_N(p_C^2 r_C + p_F^2 r_F) + r_F r_C(p_F - p_C)^2]/r_{FN}$ [12,43], in which $r_{FN} = r_F + r_N + r_C$, p_F is the spin polarization of FM, and p_C is the spin polarization of the interfacial conductivity. The spin resistance in the NM(FM) is defined as $r_{N(F)} = \rho_{N(F)} l_{sN(F)}$. $\rho_{N(F)}$ and $l_{sN(F)}$ are the resistivity and spin diffusion length of NM(FM), respectively. Because $r_N, r_F \ll r_C$ for metals, $r \approx r_C + r_N p_C^2 + r_F(p_F - p_C)^2$. As one increases a field perpendicular to the spin polarization in the NM, the spin accumulation dephases. The dephasing process in the NM and FM could be simulated by the Landau-Lifshitz-Bloch equation whose results indicate that r_N vanishes due to the Hanle effect while the r_F is preserved by the effective field of about 10^7 Oe due to Heisenberg exchange coupling [44,45] and will not contribute to the field dependence

[*]wancaihua@iphy.ac.cn
[†]xfhan@iphy.ac.cn

of real contact resistance. This gives rise to a MR whose ratio is equal to $[r(\text{High field}) - r(0)]/r(0) \approx -r_N p_C^2/r_C < 0$. This negative spin-injection-induced MR (SIMR) ratio, denoted as δ^{SI}, has been utilized in three-terminal geometries to measure τ_s in semiconductors [36–39] but is negligible in metallic systems, since $r_N \ll r_C$ by several orders of magnitude. Besides, r_C can also exhibit a field dependence due to SOC in FM/barrier/NM junctions [46,47]. This so-called tunneling anisotropic MR (TAMR) [48], whose ratio is denoted as δ^{TA}, further complicates the analysis.

Here, we will show that even with a three-terminal geometry, SIMR can be clearly observed by second-harmonic voltage measurements, since TAMR only dominates the first-harmonic voltages. We adopted this method to determine τ_s in Pt and Ta and also their corresponding temperature dependences.

II. THEORY

First we discuss the basic concept of these measurements. The tunneling conductance $g_C = 1/r_C$ is composed by counterparts for opposite spin channels, $g_C = g_{C\uparrow} + g_{C\downarrow}$. Here we have already neglected r_N and r_F in the contact resistance due to the fact that r_N, $r_F \ll r_C$. Spin injection into the NM or spin extraction from the NM induces a nonequilibrium spin accumulation μ_N in the NM, which increases or decreases Fermi levels of opposite spin channels. This can further lead to a change of g_C by $\triangle g_C = \frac{dg_{C\uparrow}}{dE}\mu_N - \frac{dg_{C\downarrow}}{dE}\mu_N = \frac{d(g_{C\uparrow}-g_{C\downarrow})}{dE}\mu_N$. The spin accumulation is given by $\mu_N = pr_N j$, where p and j are the tunneling spin polarization and current density across the junction [43]. Thus $\triangle g_C = \alpha pr_N j$ with $\alpha \equiv \frac{d(g_{C\uparrow}-g_{C\downarrow})}{dE}$. The voltage across the junction $v = r_C j$ is then

$$v = \frac{1}{(g_{C,0} + \triangle g_C)}j \approx \left(\frac{1}{g_{C,0}} - \frac{\triangle g_C}{g_{C,0}^2}\right)j$$
$$= \frac{1}{g_{C,0}}j - \frac{\alpha pr_N}{g_{C,0}^2}j^2. \tag{1}$$

Here $g_{C,0}$ is the contact conductance at zero current, or $v = r_{C,0}j - \alpha pr_N r_{C,0}^2 j^2$ with $r_{C,0}$ being the contact resistance at zero current. $r_{C,0}$ does not contain δ^{SI}. Assuming that $r_{C,0} = r_{C,00}(1 + \delta^{TA})$ and $r_N = r_{N,0}(1 + \delta^{SI})$ results in $v = r_{C,00}(1 + \delta^{TA})j - \alpha pr_{N,0}r_{C,00}^2(1 + \delta^{SI})(1 + \delta^{TA})^2 j^2$, where $r_{C,00}$ and $r_{N,0}$ are the contact resistance and spin resistance at $H = 0$ and $j = 0$, respectively. This equation can be further reduced considering $\delta^{TA} \ll 1$ and $\delta^{SI} \ll 1$:

$$v \approx r_{C,00}(1 + \delta^{TA})j - \alpha pr_{N,0}r_{C,00}^2$$
$$\times (1 + \delta^{SI} + 2\delta^{TA})j^2. \tag{2}$$

In practice, an AC current $j = j_0 \sin(\omega t)$ satisfying $\triangle g_C < g_{C,0}/10$ was selected to make the above Taylor expansion reasonable. Thus $v_{1\omega} = r_{C,00}(1 + \delta^{TA})j_0$ has no explicit dependence on SIMR while $v_{2\omega} = \frac{1}{2}\alpha pr_{N,0}r_{C,00}^2(1 + \delta^{SI} + 2\delta^{TA})j_0^2$ has a dependence on both δ^{SI} and $2\delta^{TA}$. They also differ in phase by $90°$. We would expect that δ^{TA} dominates in $v_{1\omega}$ while SIMR becomes comparable to the δ^{TA} and thus observable in $v_{2\omega}$ as shown in the following experiments.

III. METHODS

Stacks of SiO$_2$/Ta(10) or Pt(10)/MgO(2)/Co$_{40}$Fe$_{40}$B$_{20}$(4)/Ta(5)/Ru(7) (thickness in nm) provided by Singulus Technologies AG were deposited via magnetron sputtering and then postannealed with a magnetic field of 1 T along the x axis at 300 ^oC for 1 h to induce an easy axis along the x axis. M-H curves acquired by a vibrating sample magnetometer (Microsense) showed in-plane magnetic anisotropy for both Ta/MgO/CoFeB and Pt/MgO/CoFeB stacks [Figs. 1(a) and 1(b)]. The anisotropy field of each sample is about 15 kOe along the z axis, while the easy axis is along the x axis. H_x smaller than 1 kOe is sufficient to align the magnetization along the easy axis.

The extended films were then processed into magnetic tunneling junctions by ultraviolet lithography and argon ion etching. The junctions had one top electrode (E1) and three bottom ones (E2, E3, and E4) [Figs. 1(c) and 1(d)]. The size of the junctions was 6 μm × 6 μm. Ta/MgO/CoFeB or Pt/MgO/CoFeB junctions were surrounded by MgAlO$_x$ for protection and also for isolating E1 from the remaining electrodes. Magnetotransport properties were measured in a physical property measurement system (Quantum Design-9T). To measure the inverse spin Hall effect (ISHE) of the bottom electrodes, an AC current with sine wave and $f = \omega/2\pi = 8.7$ Hz was applied between E1 and E3 using a Keithley 6221 and the first-harmonic voltage $V_{1\omega}$ between E2 and E4 was first preamplified (Stanford Research, SR560) and then picked up by a lock-in amplifier (SR830) [Fig. 1(d)].

IV. RESULTS AND DISCUSSIONS

In this setup, spin-polarized current was perpendicularly injected from the FM to the NM. Their spin orientation was along the x axis at $|H_x| > 500$ Oe. Then a voltage in the open circuit can be detected along the y axis due to the ISHE. The field dependences of the first-harmonic voltage $V_{1\omega}^{\text{ISHE}}$ between E2 and E4 in Ta and Pt junctions are illustrated in Figs. 1(e) and 1(f). The sign of $V_{1\omega}^{\text{ISHE}}$ reverses as expected with the reversed sign of H_x. $V_{1\omega}^{\text{ISHE}}$ has opposite signs in the Ta and Pt due to their opposite θ_{SH} [49,50], which indicates successful spin injection into the bottom heavy metal layer. Similar ISHE behaviors in both junctions have also been observed near room temperature. The maximum $V_{1\omega}^{\text{ISHE}}/j_0$ of Ta and Pt junctions is about 1 and 0.1 mΩ at high temperature, respectively, which is in the same order of magnitude as in Ref. [51].

Three-terminal tunneling magnetoresistance (TMR) measurements are further performed on both Ta and Pt junctions. We have first detected the first-harmonic voltage $V_{1\omega}^{3T}$ between E1 and E4 with an AC current applied between E1 and E3 [inset of Fig. 2(a)]. First harmonic TMR ratio $\delta_{1\omega}$ is defined as $[V_{1\omega}^{3T}(H)$-$V_{1\omega}^{3T}(0)]/V_{1\omega}^{3T}(0)$ and its field dependences is shown in Figs. 2(a) to 2(d). The MR originates from the tunneling junction instead of the anisotropic magnetoresistance (AMR) of the CoFeB layer. Direct measurements of AMR of the Ta/MgO/CoFeB and Pt/MgO/CoFeB stacks showed negligible field dependence in the first- and second-harmonic measurements. AMR only appears in the DC measurement, whose value is only about 0.05% at room temperature. Bear in mind
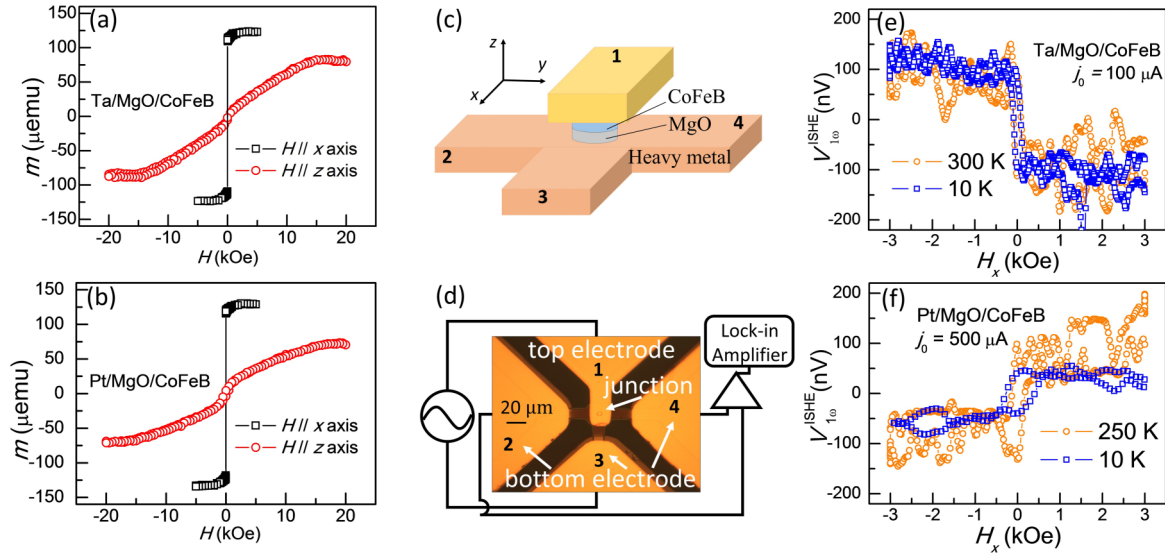
FIG. 1. (a),(b) Magnetic moment m vs H curves of Ta/MgO/CoFeB and Pt/MgO/CoFeB films. (c) Schematic of heavy metal/MgO/$Co_{40}Fe_{40}B_{20}$ junctions. Top electrode 1 (E1) and bottom electrodes 2, 3, and 4 (E2, E3, and E4) are on opposite sides of 40-nm $MgAlO_x$ around the tunnel junction area. (d) The ISHE measurement setup applying an AC current between E1 and E3 and detecting the voltage between E2 and E4 with a preamplifier and a lock-in amplifier. (e),(f) First harmonic ISHE voltages of Ta/MgO/CoFeB and Pt/MgO/CoFeB. High (orange circle) and low temperature (blue) data are shown together for the Ta and Pt stacks. The current amplitude is 100 for Ta and 500 μA for Pt. Opposite field dependences in (e) and (f) indicate different signs of θ_{SH} of Ta and Pt.

that the resistance of the tunnel junction is much higher than the resistance of the CoFeB thin film. Thus the voltage variation caused by the AMR of the CoFeB film only is too tiny to explain the field-dependence of $V_{1\omega}^{3T}$. Here the TMR is mainly attributed to TAMR of the CoFeB/MgO/heavy metal junctions, and we use δ^{TA} instead of δ in the following analysis.
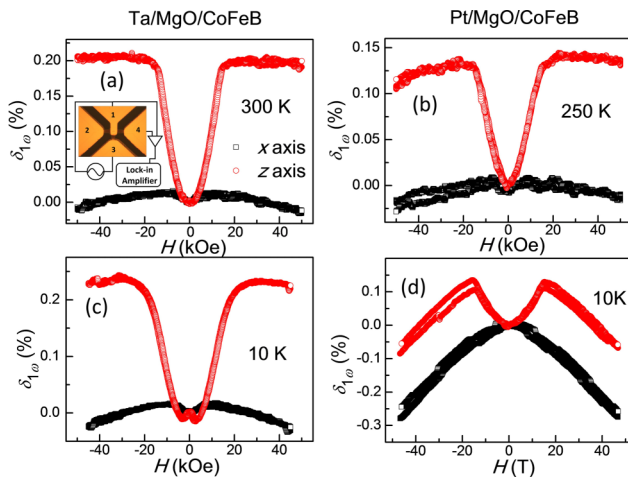
FIG. 2. Tunneling magnetoresistance (TMR) ratio obtained from the first-harmonic voltage with the three-terminal (3T) measurement setup applying AC currents between E1 and E3 and detecting the voltages between E1 and E4 in the inset at high temperatures (a) 300 for Ta/MgO/CoFeB and (b) 250 K for Pt/MgO/CoFeB, or low temperature 10 K for (c) Ta/MgO/CoFeB and (d) Pt/MgO/CoFeB. The external field is either in the plane along the x axis (black square) or out of plane along the z axis (red circle). The currents are identical as in Figs. 1(e) and 1(f), 100 for Ta/MgO/CoFeB [(a) or (c)] and 500 μA for Pt/MgO/CoFeB [(b) or (d)].

At high temperature, $\delta_{1\omega}^{TA}(z)$ first quadratically increases as H_z increases from zero in both Ta and Pt junctions [Figs. 2(a) and 2(b)] and later gradually saturates at 0.20% for the Ta and 0.14% for the Pt junction as H_z approaches 15 kOe which is also the anisotropy field of the CoFeB layer. Further increasing H_z leads to a MR reduction for both junctions. When H_x is applied, $\delta_{1\omega}^{TA}(x)$ increases only by about 0.01% and then decreases gradually toward the negative MR. Note that $\delta_{1\omega}^{TA}(z)$ is much larger than $\delta_{1\omega}^{TA}(x)$. H_z aligns the magnetization from in-plane to out-of-plane, which subsequently changes the density of state of the interfacial FM via SOC and results in a TAMR as predicted theoretically [48,52]. The phenomenon $\delta_{1\omega}^{TA}(z) > \delta_{1\omega}^{TA}(x)$ is consistent with Ref. [53], since H_x keeps the magnetization along the easy axis, and consequently $\delta_{1\omega}^{TA}(x)$ varies little.

Similar behaviors are also observed at 10 K, except for larger saturation fields and slightly larger $\delta_{1\omega}^{TA}(z)$ values [Figs. 2(c) and 2(d)]. The negative MR ratio, which depends on the applied field instead of magnetization, is also observed at 10 K. For an explicit discussion, the $\delta_{1\omega}^{TA}(z)$ vs H_z curve in Fig. 2(c) can be fitted with the three contributions as plotted in Fig. 3 as curves α, β, and γ. The curve γ is the contribution of the mentioned negative MR ratio at large field. This MR might originate from suppression of electron-magnon scattering [54,55] or weak localization [56,57] of electrodes. Though the detailed mechanism is still unclear, the negative MR ratio is also observed in this kind of NM/MgO/CoFeB structure. TAMR in the work of Park et al. [58] also declines after reaching a maximum at the saturation field. The curve β, due to TAMR, is highly relevant to magnetization and can be reproduced by $aR_{xy}^2(H)$ with a being the proportional coefficient. The curve α shows a small negative MR ratio (about −0.014%) that appears at low H_z in the Ta junction, which is the only remarkable difference between the results
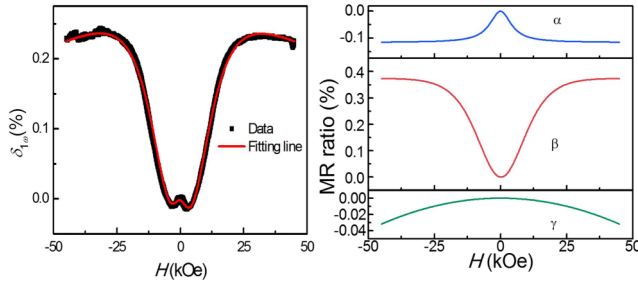
FIG. 3. (a) The fitting of the $\delta_{1\omega}^{TA}(z)$ vs H_z curve. (b) Three contributions, Hanle effect (curve α), TAMR (curve β), and a negative MR (curve γ), are taken into account.

FIG. 4. Second-harmonic voltage with the three-terminal (3T) measurement setup for Ta/MgO/CoFeB at (a) 300 and (b) 10 K, and for Pt/MgO/CoFeB at (c) 250 and (d) 10 K. The magnetic field was applied along the x axis (black square) for the inverted Hanle measurement and the z axis (red circle) for the Hanle measurement.

of 10 K and high temperature. This negative MR ratio exhibits a similar field dependence as the Hanle-effect-induced SIMR which would exhibit a Lorentzian-shape dependence as discussed next. Thus we attribute it to spin injection into Ta. This $\delta_{1\omega}^{SI}$ should have been negligibly small due to the fact that $r_N \ll r_C$. In fact, it turns out to be unobservable in the Pt junction or at high temperatures. It might be possible that inhomogeneities of the MgO layer which is shown in Appendix A result in a significant reduction of the effective tunneling area and smaller r_C in the Ta junction. This may lead to a reemerging of $\delta_{1\omega}^{SI}$ although $\delta_{1\omega}^{SI}$ is still one order smaller than $\delta_{1\omega}^{TA}(z)$. Inhomogeneous current distribution due to the resistance of the nonmagnetic layer within the junction area could reduce the measured tunneling resistance below the real tunneling resistance by about 10.8% and 4.5% for Ta and Pt junctions, respectively, due to device geometry as well as inhomogeneous current distribution within the junction [59,60]. However, this would not affect the injected spins and their dephasing process in the heavy metal layers. Therefore, this resistance adjustment would not physically influence the field dependence of the TAMR and the SIMR effects which is the basis of estimating the spin relaxation times.

$V_{2\omega}^{3T}$ was detected in the same setup as shown in the inset of Fig. 2(a). The only difference is that the second-harmonic voltage with a 90° phase shift was measured with the lock-in amplifier. As shown in Eq. (2), δ^{SI} should be comparable to δ^{TA} within a factor of 2 for the second-harmonic signal. Thus this method renders Hanle and inverted Hanle effect signals induced by SIMR detectable even in the presence of a TAMR background (Fig. 4).

The field dependence of $V_{2\omega}^{3T}$ at 300 or 250 K for the Ta and Pt junction is shown in Figs. 4(a) and 4(c). For small H_z, the magnetization is still aligned along the easy axis. An AC current injects (extracts) spins into (from) the NM and leads to a nonequilibrium spin accumulation, which conversely influences tunneling resistance and contributes an additional $V_{2\omega}$. A vertical H_z can dephase the spin accumulation via the Hanle effect and therefore diminishes the additional $V_{2\omega}$, leading to a negative MR with a Lorentzian shape in the second-harmonic signal. This Hanle dephasing is the same as established by Johnson and Silsbee [61] for a DC measurement. It is worth noting that $\delta_{2\omega}^{TA}$ and $\delta_{2\omega}^{SI}$ contribute to a positive and negative MR, respectively. In addition, $\delta_{2\omega}^{TA}$ as well as curve γ has a H_z^2 dependence at low field. Thus by fitting $V_{2\omega}$ vs H_z curves with a Lorentzian function plus a H_z^2 function, we can obtain a spin relaxation time $\tau_s = e/(m_e B_0)$
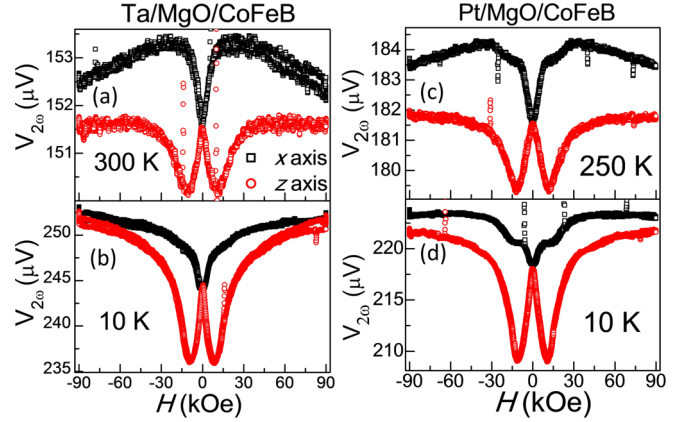
with the electron charge e, electron mass m_e, and B_0 being the half-width at half maximum of the Lorentzian fitting. τ_s is (7.8 ± 1.6) at 300 and (13.1 ± 0.6) ps at 10 K for Ta [Figs. 4(a) and 4(b)]. By further increasing H_z beyond 10 kOe, $V_{2\omega}^{3T}$ increases due to both the tilting of magnetization and the concomitant TAMR contribution.

In contrast, H_x avoids dephasing of the spin polarization along x, and therefore extends the spin relaxation process and finally causes a positive MR in small field. This picture accounts for the inverted Hanle effect [40]. A similar positive δ^{SI} also occurs as applying H_x for the second-harmonic signal (Fig. 4, black square). Besides, $V_{2\omega}$ exhibits a $H_{z/x}$ dependence at high fields, especially at 10 K, but the origin of this field dependence is unclear at this point. The Hanle signal in Figs. 4(c) and 4(d) results in τ_s (5.0 ± 1.5) at 250 and (7.3 ± 0.6) ps at 10 K for Pt. The inverted Hanle SIMR shows similar behavior for Ta. More than four devices are measured to estimate the τ_s for each type of stack.

In order to investigate the temperature T dependence of τ_s, we have conducted the second-harmonic SIMR measurement in a Hanle geometry at different temperatures [Figs. 5(a) and 5(b)]. As T decreases from 300 to 10 K, the Hanle-effect-induced $\triangle V_{2\omega}$ grows significantly by nearly one order of magnitude. In order to examine whether the field range for selecting the data affects B_0, we have tried different ranges (± 13, ± 14, and ± 15 kOe) for the fitting. The T dependence is basically the same for different fitting ranges. Their variance is less than 2 ps for both materials. Taking the ± 14 kOe fitting range, τ_s in Ta gradually decays from (13.1 ± 0.6) at 10 to (7.8 ± 1.6) ps at 300 K. In contrast, if the H^2 correction is ignored in the fitting, τ_s stays at 20 below 150 and then decays to 14 ps at 300 K. These values are not only 50% higher than those with the H^2 correction but also exhibit an unreasonable T dependence. Thus the H^2 correction is indispensable. τ_s of Pt and Ta is about 10 ps or below. These values are one to three orders smaller than τ_s in light metals or semiconductors, consistent with the trend that elements with larger atomic number have stronger SOC. $\tau_{s,Pt}$ is about half of $\tau_{s,Ta}$ at all temperatures in our experiment and much smaller than $\tau_{s,Au}$ of 45 ps. Here $\tau_{s,Pt} = (3.8 \pm 0.5)$ ps at 300 K is
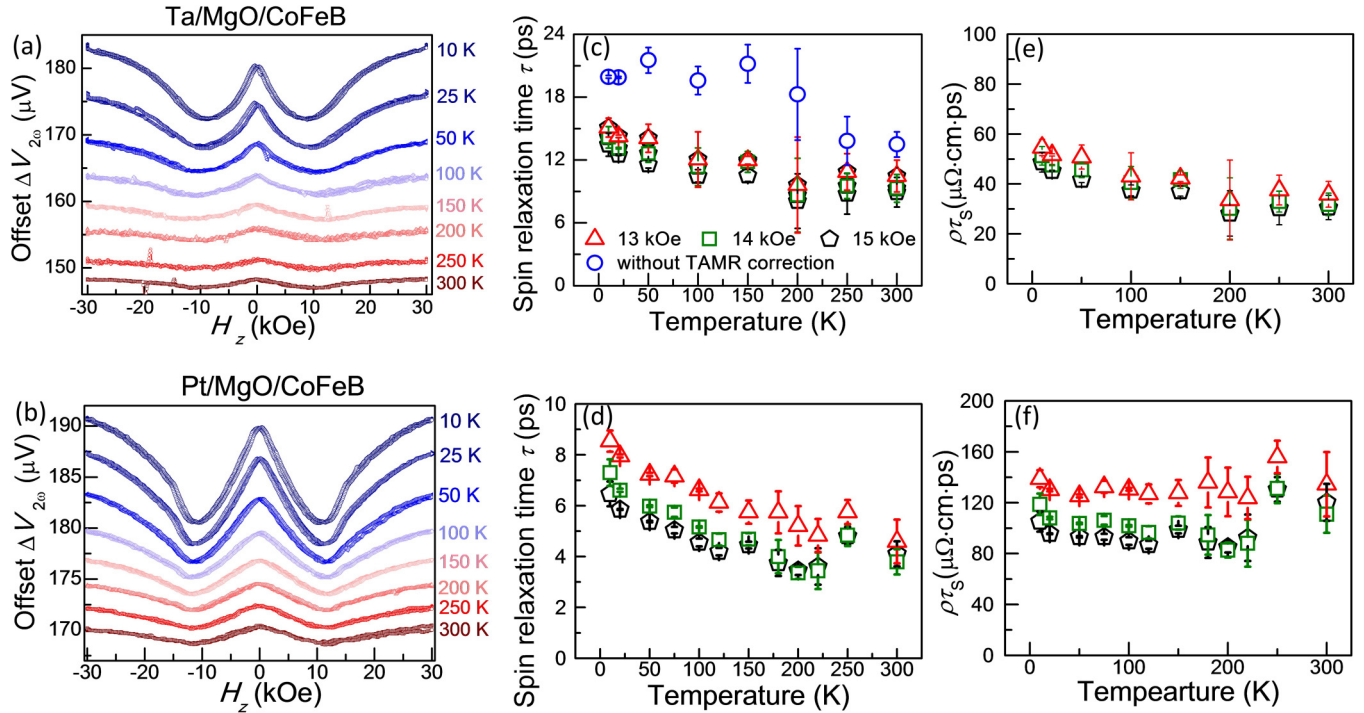
FIG. 5. Temperature dependence of the second-harmonic voltage of Hanle measurements for (a) Ta/MgO/CoFeB and (b) Pt/MgO/CoFeB from 10 to 300 K. Temperature dependence of spin relaxation time (c) for Ta/MgO/CoFeB and (d) for Pt/MgO/CoFeB acquired via fitting the data with a Lorentzian curve plus a parabolic function for the TAMR correction applied in different field ranges ± 13 Oe (red triangle), ± 14 Oe (olive square), and ± 15 Oe (black pentagon) or without the parabolic function fitting (blue circle). (e) This panel shows that $\tau_s \rho$ of Pt remains nearly constant from 300 to 10 K for all fitting ranges. (f) Temperature dependence of $\tau_s \rho$ of Ta.

about twice of 1.9 ps measured by the Hanle MR, which might be caused by lower resistivity in the former Pt and different film thicknesses in the two experiments. In our experiment, $\rho_{Pt} = 24.4 \, \mu\Omega$ cm at 300 K, while it is 58 $\mu\Omega$ cm in Ref. [28]. $\tau_s \rho$ appears to be a constant for these two samples. The T dependence of ρ_{Pt} and ρ_{Ta} is also measured. For the resistivity measurement, the top structure MgO/CoFeB/capping layers in the Ta/MgO/CoFeB or Pt/MgO/CoFeB stacks are etched away. ρ_{Pt} decreases weakly with decreasing temperature and $\tau_s \rho$ in Pt is nearly a constant from 300 to 10 K for all the fitting ranges [Fig. 5(f)]. The momentum relaxation time τ_p is inversely proportional to ρ. Thus τ_s / τ_p is also a constant, which indicates that the spin relaxation in Pt is governed by the Elliott-Yafet mechanism [12]. We also applied a THz technique [62] to directly measure momentum relaxation time and resistivity of Pt with a 30 nm thickness, which gives $\tau_p = (5 \pm 3)$ fs and $\rho_{Pt} = 16 \, \mu\Omega$ cm at 300 K. Assuming that τ_p is proportional to $1/\rho_{Pt}$, τ_p in our Pt/MgO/CoFeB stacks is thus around 2.7 fs. Therefore the spin flip probability of each scattering τ_p / τ_s is around 7×10^{-4} for Pt at 300 K.

Our ρ_{Ta} is about 342 $\mu\Omega$ cm at 300 K, much larger than those reported for the resistivity of the α-phase and even β-phase Ta or amorphous Ta [63–68], which might be due to oxidation of Ta after the top structure is etched. Schwartz *et al.* [66] reported a resistivity at room temperature of $200 \pm 20 \, \mu\Omega$ cm and a temperature coefficient of resistance (TCR) from 200 to 300 K of -175 to -178 p.p.m./K for β Ta. Before his work, Schauer *et al.* [65] also reported a TCR of about -100 p.p.m./K for β Ta. In 2006, Narayan *et al.* [67] reported a room-temperature resistivity of 275 $\mu\Omega$ cm for amorphous

Ta and the negative TCR of about -205 p.p.m./K. According to Naranyan *et al.* [67] and Stella *et al.* [68], the amorphous Ta has a higher resistivity (above 200 $\mu\Omega$ cm) and a negative TCR. In our films, the TCR is -198 p.p.m./K for Ta film. Although the TCR of our sample is in the same level of magnitude as the reported ones, the resistivity is too high to eliminate the possibility of oxidation. The interface oxidation layer would make the effective cross-sectional area less than the nominal one which is used to calculate the resistivity, which would enlarge the resistivity but not the TCR of the films because the oxide of tantalum nearly does not participate in the electrical transport. Therefore $\rho_{Ta}\tau_{s,Ta}$ vs T shown in Fig. 5(e) is not used here for examining the spin relaxation mechanism.

V. CONCLUSIONS

In conclusion, TAMR dominates the first-harmonic three-terminal MR measurement while SIMR becomes significant compared to the TAMR background and turns out to be much easier measured in the second- than in the first-harmonic signal. This renders conventional three-terminal FM/barrier/NM devices suitable for directly measuring the spin relaxation time τ_s of heavy metals without complications from proximity effects [69–72] that occur when the heavy metal is in direct contact with a ferromagnet. The ISHE is also observed, which proves successful spin injection into Ta and Pt. By fitting Hanle curves with a Lorentzian function plus a parabolic TAMR background, we have obtained τ_s of Ta and Pt. The τ_s for both materials exhibits a small increase from 300 to 10 K, such that τ_s is about (7.8 ± 1.6) and (5.0 ± 1.5) ps for Ta

and Pt at high temperature while it is about (13.1 ± 0.6) and (7.3 ± 0.6) ps at 10 K, respectively. Since $\tau_s\rho$ stays constant at all temperatures, the spin relaxation in Pt seems to be dominated by the Elliott-Yafet mechanism. This experimental approach provides an electrical manner to directly quantify the spin relaxation time of heavy metals, which have been elusive from conventional SIMR or optical measurements. Furthermore, there is no physical limitation for this method to be generalized to other light metals and semiconductors.

APPENDIX A: TEM CHARACTERIZATION OF THE CROSS SECTION OF JUNCTIONS

TEM pictures (Fig. 6) show the good quality of the MgO layer with clear and flat interfaces in large scales [Figs. 6(a) and 6(b) for Ta/MgO/CoFeB stacks and Figs. 6(d) and 6(e) for Pt/MgO/CoFeB stacks], demonstrating that a portion of samples, at least in probability, are good enough for direct tunneling to dominate the field dependence of the junction resistance in the harmonic measurement. This means multimeasurement in different samples would be helpful to obtain more reliable τ values.

Nevertheless, Figs. 6(c) and 6(f) also show that the MgO thickness in some region is not very uniform. The yellow arrows point out the area where the thickness is less than surrounding area and could probably act as the inhomogeneous area which leads to a larger tunneling rate and may account for a reduction of the effective tunneling area.

APPENDIX B: *I-V* CHARACTERISTICS

This section shows the *I-V* characteristics of Ta/MgO/CoFeB and Pt/MgO/CoFeB junctions at room temperature [Figs. 7(a) and 7(b)].

Brinkman *et al.* (BDR fit) [73] gave the equation for the conductivity of the metal-insulator-metal junctions as
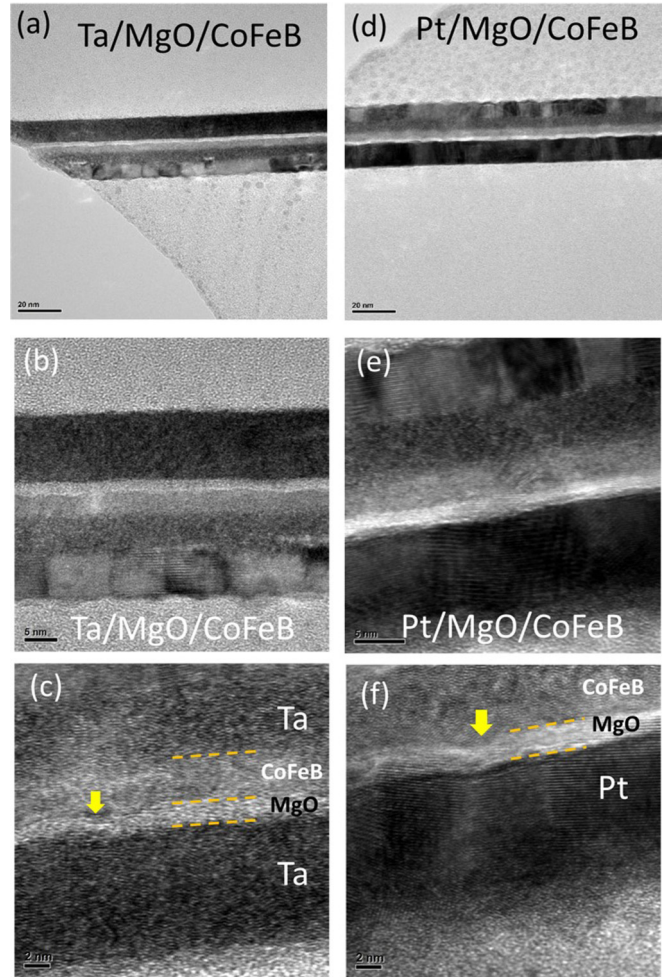
FIG. 6. (a)–(c) TEM pattern of the cross section of Ta/MgO/CoFeB stacks in different scales. (d)–(f) TEM pattern of the cross section of Pt/MgO/CoFeB stacks in different scales. Yellow arrows in the patterns point to the inhomogeneous area of the MgO barrier.

$[G(V)]/[G(0)] = 1 - AV + BV^2$ at low voltages, in which A and B are material related parameters. The equation indicates that the plot of conductivity vs voltage will be a parabolic function. We adopt the parabolic fitting to our dI/dV-V data as shown in Figs. 7(c) and 7(d). The data show good fitting outcomes, indicating the tunneling mechanism dominates transport properties of the junctions.

APPENDIX C: THE CURRENT DEPENDENCE OF FIRST- AND SECOND-HARMONIC VOLTAGES

We measured the current dependence of first- and second-harmonic voltages shown in Figs. 8 and 9 to demonstrate that the first- and second-harmonic voltage variations are proportional to j and j^2, respectively. The obtained τ_s stays almost the same in the current ranges we used for both Ta and Pt samples. Due to a much lower signal-to-noise ratio at small measurement current, τ_s shows some abnormality in this region, which we think is not physical.
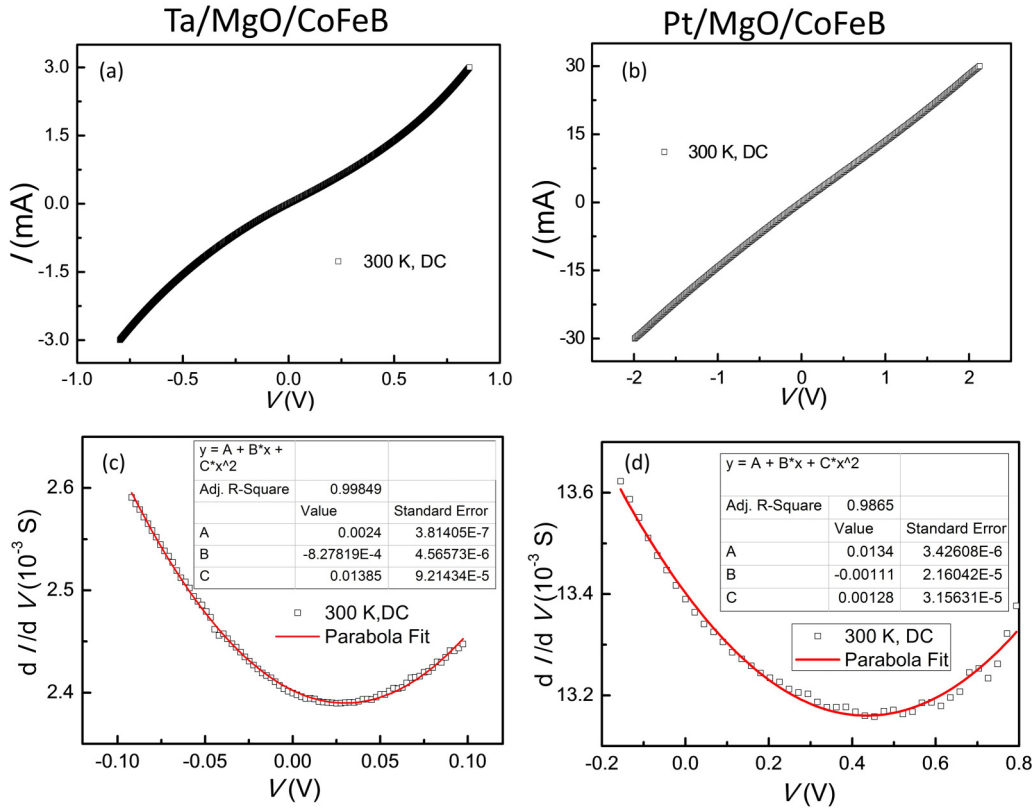
FIG. 7. I-V curves of (a) Ta/MgO/CoFeB and (b) Pt/MgO/CoFeB junctions at room temperature. Voltage dependence of conductance of (c) Ta/MgO/CoFeB and (d) Pt/MgO/CoFeB junctions at room temperature at low voltage. The red lines are parabolic fittings whose parameters are shown in the insets in the figures.
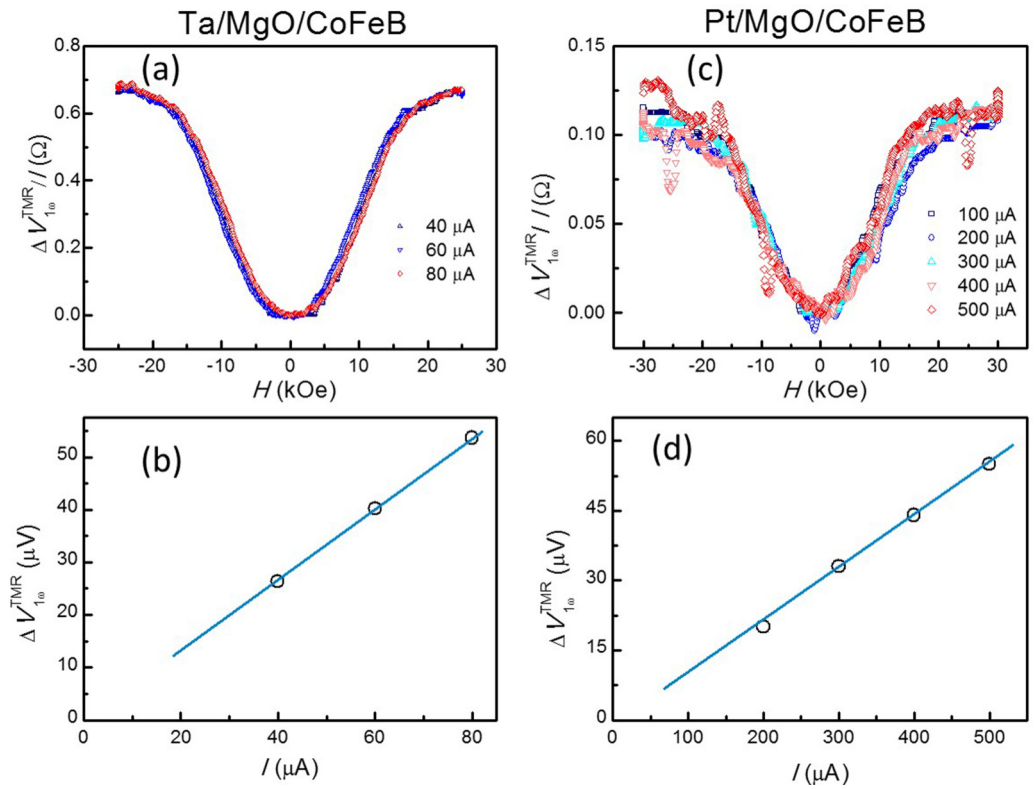
FIG. 8. (a),(c) The field dependence of $\Delta V_{1\omega}^{\text{TMR}}/I$ under different applied currents; and (b),(d) the dependence of $\Delta V_{1\omega}^{\text{TMR}}$ on the applied current for Ta/MgO/CoFeB samples [(a) and (b)] and Pt/MgO/CoFeB samples [(c) and (d)].
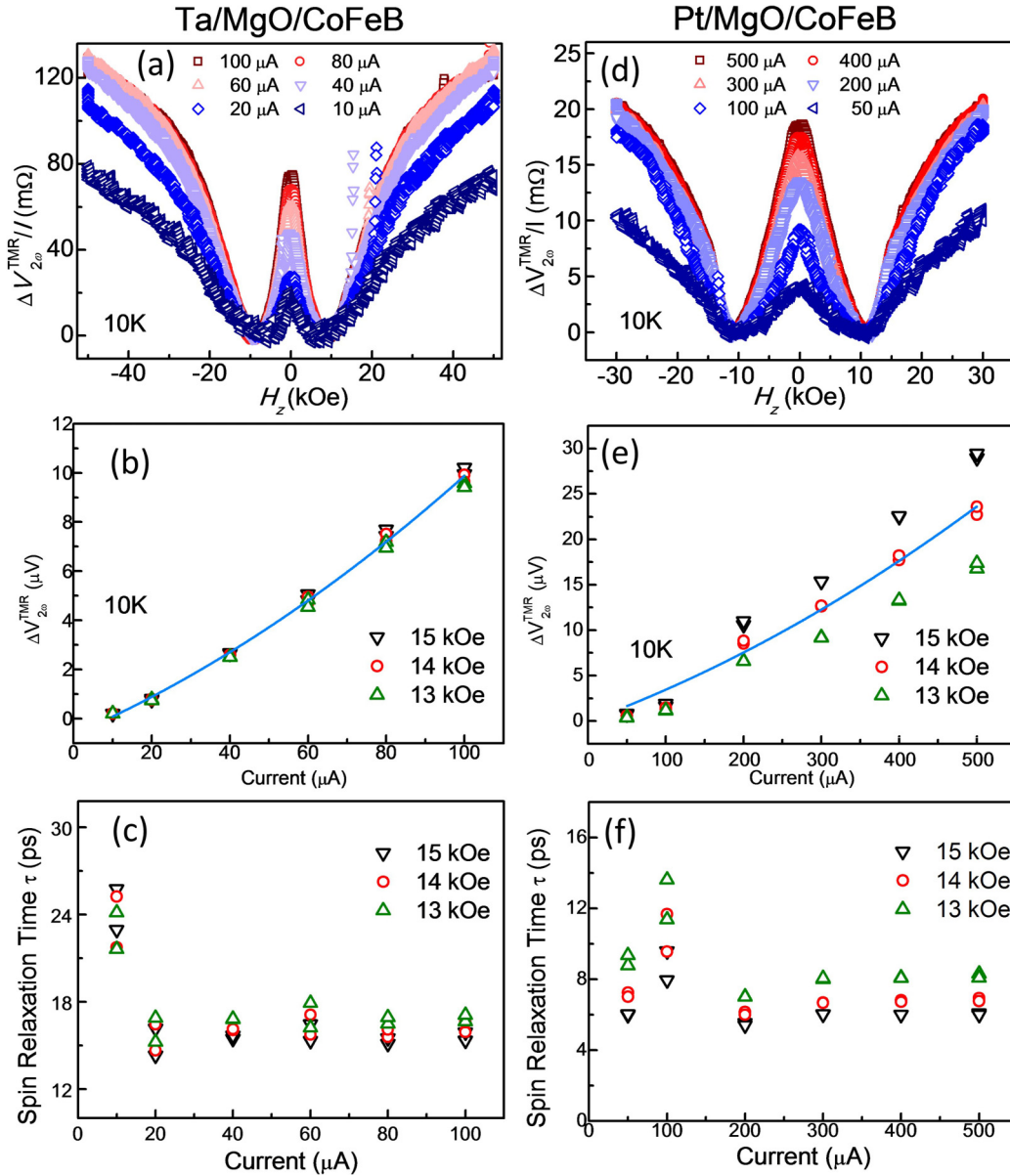
FIG. 9. (a),(d) The field dependence of $\Delta V_{2\omega}^{\mathrm{TMR}}/I$ under different applied currents; (b),(e) the current dependence of $\Delta V_{2\omega}^{\mathrm{TMR}}$; and (c),(f) the τ measured at different currents for Ta/MgO/CoFeB samples [(a)–(c)] and Pt/MgO/CoFeB samples [(d)–(f)].

[1] C. O. Avci, K. Garello, I. M. Miron, G. Gaudin, S. Auffret, O. Boulle, and P. Gambardella, Appl. Phys. Lett. **100**, 212404 (2012).

[2] G. Finocchio, M. Carpentieri, E. Martinez, and B. Azzerboni, Appl. Phys. Lett. **102**, 212410 (2013).

[3] E. Martinez, S. Emori, and G. S. D. Beach, Appl. Phys. Lett. **103**, 072406 (2013).

[4] C. H. Sim, J. C. Huang, M. Tran, and K. Eason, Appl. Phys. Lett. **104**, 012408 (2014).

[5] P. V. Ong, N. Kioussis, P. K. Amiri, K. L. Wang, and G. P. Carman, J. Appl. Phys. **117**, 17B518 (2015).

[6] P. M. Haney, H. W. Lee, K. J. Lee, A. Manchon, and M. D. Stiles, Phys. Rev. B **88**, 214417 (2013).

[7] K. K. Meng, J. Miao, X. G. Xu, J. X. Xiao, J. H. Zhao, and Y. Jiang, Phys. Rev. B **93**, 060406 (2016).

[8] S. Y. Huang, X. Fan, D. Qu, Y. P. Chen, W. G. Wang, J. Wu, T. Y. Chen, J. Q. Xiao, and C. L. Chien, Phys. Rev. Lett. **109**, 107204 (2012).

[9] A. Hoffmann and S. D. Bader, Phys. Rev. Appl. **4**, 047001 (2015).

[10] W. J. Kong, Y. R. Ji, X. Zhang, H. Wu, Q. T. Zhang, Z. H. Yuan, C. H. Wan, X. F. Han, T. Yu, K. Fukuda, H. Naganuma, and M. J. Tung, Appl. Phys. Lett. **109**, 132402 (2016).

[11] X. Zhang, C. H. Wan, Z. H. Yuan, Q. T. Zhang, H. Wu, L. Huang, W. J. Kong, C. Fang, U. Khan, and X. F. Han, Phys. Rev. B **94**, 174434 (2016).

[12] I. Žutić, J. Fabian, and S. D. Sarma, Rev. Mod. Phys. **76**, 323 (2004).

[13] W. Zhang, V. Vlaminck, J. E. Pearson, R. Divan, S. D. Bader, and A. Hoffmann, Appl. Phys. Lett. **103**, 242414 (2013).

[14] O. Mosendz, V. Vlaminck, J. E. Pearson, F. Y. Fradin, G. E. W. Bauer, S. D. Bader, and A. Hoffmann, Phys. Rev. B **82**, 214403 (2010).

[15] V. Vlaminck, J. E. Pearson, S. D. Bader, and A. Hoffmann, Phys. Rev. B **88**, 064414 (2013).

[16] O. Mosendz, J. E. Pearson, F. Y. Fradin, G. E. W. Bauer, S. D. Bader, and A. Hoffmann, Phys. Rev. Lett. **104**, 046601 (2010).

[17] J. C. Rojas-Sanchez, N. Reyren, P. Laczkowski, W. Savero, J. P. Attane, C. Deranlot, M. Jamet, J. M. George, L. Vila, and H. Jaffres, Phys. Rev. Lett. **112**, 106602 (2014).

[18] S. Woo, M. Mann, A. J. Tan, L. Caretta, and G. S. D. Beach, Appl. Phys. Lett. **105**, 212404 (2014).

[19] K. Garello, I. M. Miron, C. O. Avci, F. Freimuth, Y. Mokrousov, S. Blugel, S. Auffret, O. Boulle, G. Gaudin, and P. Gambardella, Nat. Nanotechnol. **8**, 587 (2013).

[20] H. Reichlova, D. Kriegner, V. Holy, K. Olejnik, V. Novak, M. Yamada, K. Miura, S. Ogawa, H. Takahashi, T. Jungwirth, and J. Wunderlich, Phys. Rev. B **92**, 165424 (2015).

[21] P. Monod and F. Beuneu, Phys. Rev. B **19**, 911 (1979).

[22] S. Schultz and C. Latham, Phys. Rev. Lett. **15**, 148 (1965).

[23] R. B. Lewis and T. R. Carver, Phys. Rev. **155**, 309 (1967).

[24] A. Y. Elezzabi, M. R. Freeman, and M. Johnson, Phys. Rev. Lett. **77**, 3220 (1996).

[25] P. Riego, S. Vlez, J. M. Gomez-Perez, J. A. Arregi, L. E. Hueso, F. Casanova, and A. Berger, Appl. Phys. Lett. **109**, 172402 (2016).

[26] M. I. Dyakonov, Phys. Rev. Lett. **99**, 126601 (2007).

[27] S. Vélez, V. N. Golovach, A. Bedoya-Pinto, M. Isasa, E. Sagasta, M. Abadia, C. Rogero, L. E. Hueso, F. S. Bergeret, and F. Casanova, Phys. Rev. Lett. **116**, 016603 (2016).

[28] H. Wu, X. Zhang, C. H. Wan, B. S. Tao, L. Huang, W. J. Kong, and X. F. Han, Phys. Rev. B **94**, 174407 (2016).

[29] M. Johnson and R. H. Silsbee, Phys. Rev. Lett. **55**, 1790 (1985).

[30] F. J. Jedema, A. T. Filip, and B. J. van Wees, Nature (London) **410**, 345 (2001).

[31] F. J. Jedema, H. B. Heersche, A. T. Filip, J. J. A. Baselmans, and B. J. van Wees, Nature (London) **416**, 713 (2002).

[32] J. H. Ku, J. Chang, H. Kim, and J. Eom, Appl. Phys. Lett. **88**, 172510 (2006).

[33] O. M. J. van't Erve, A. T. Hanbicki, M. Holub, C. H. Li, C. Awo-Affouda, P. E. Thompson, and B. T. Jonker, Appl. Phys. Lett. **91**, 212109 (2007).

[34] Y. Ji, A. Hoffmann, J. S. Jiang, and S. D. Bader, Appl. Phys. Lett. **85**, 6218 (2004).

[35] Y. Ji, A. Hoffmann, J. E. Pearson, and S. D. Bader, Appl. Phys. Lett. **88**, 052509 (2006).

[36] S. P. Dash, S. Sharma, R. S. Patel, M. P. de Jong, and R. Jansen, Nature (London) **462**, 491 (2009).

[37] K. R. Jeon, B. C. Min, I. J. Shin, C. Y. Park, H. S. Lee, Y. H. Jo, and S. C. Shin, Appl. Phys. Lett. **99**, 199902 (2011).

[38] X. Lou, C. Adelmann, M. Furis, S. A. Crooker, C. J. Palmstrom, and P. A. Crowell, Phys. Rev. Lett. **96**, 176603 (2006).

[39] T. Uemura, K. Kondo, J. Fujisawa, K. Matsuda, and M. Yamamoto, Appl. Phys. Lett. **101**, 132411 (2012).

[40] S. P. Dash, S. Sharma, J. C. L. Breton, J. Peiro, H. Jaffrès, J. M. George, A. Lemaitre, and R. Jansen, Phys. Rev. B **84**, 054410 (2011).

[41] S. Singh, J. Katoch, J. S. Xu, C. Tan, T. C. Zhu, W. Amamou, J. Hone, and R. Kawakami, Appl. Phys. Lett. **109**, 122411 (2016).

[42] S. Garzon, I. Žutić, and R. A. Webb, Phys. Rev. Lett. **94**, 176601 (2005).

[43] A. Fert and H. Jaffrès, Phys. Rev. B **64**, 184420 (2001).

[44] B. D. Cullity and C. D. Graham, *Introduction to Magnetic Materials* (John Wiley & Sons, Inc., Hoboken, NJ, 2008), pp. 115–149.

[45] I. M. Miron, K. Garello, G. Gaudin, P. J. Zermatten, M. V. Costache, S. Auffret, S. Bandiera, B. Rodmacq, A. Schuhl, and P. Gambardella, Nature (London) **476**, 189 (2011).

[46] A. Matos-Abiague and J. Fabian, Phys. Rev. B **79**, 155303 (2009).

[47] O. Txoperena, M. Gobbi, A. Bedoya-Pinto, F. Golmar, X. N. Sun, L. E. Hueso, and F. Casanova, Appl. Phys. Lett. **102**, 192406 (2013).

[48] C. Gould, C. Ruster, T. Jungwirth, E. Girgis, G. M. Schott, R. Giraud, K. Brunner, G. Schmidt, and L. W. Molenkamp, Phys. Rev. Lett. **93**, 117203 (2004).

[49] C. Hahn, G. de Loubens, O. Klein, M. Viret, V. V. Naletov, and J. B. Youssef, Phys. Rev. B **87**, 174417 (2013).

[50] A. Hoffmann, IEEE Trans. Magn. **49**, 5172 (2013).

[51] L. Liu, C.-T. Chen, and J. Z. Sun, Nat. Phys. **10**, 561 (2014).

[52] H. Saito, S. Yuasa, and K. Ando, Phys. Rev. Lett. **95**, 086604 (2005).

[53] S. Hatanaka, S. Miwa, K. Matsuda, K. Nawaoka, K. Tanaka, H. Morishita, M. Goto, N. Mizuochi, T. Shinjo, and Y. Suzuki, Appl. Phys. Lett. **107**, 082407 (2015).

[54] B. Raquet, M. Viret, E. Sondergard, O. Cespedes, and R. Mamy, Phys. Rev. B **66**, 024433 (2002).

[55] P. V. P. Madduri and S. N. Kaul, Phys. Rev. B **95**, 184402 (2017).

[56] G. Bergmann, Phys. Rep. **107**, 1 (1984).

[57] R. S. Markiewicz and C. J. Rollins, Phys. Rev. B **29**, 735 (1984).

[58] J.-Y. Park, S.-h. C. Baek, S.-Y. Park, Y. Jo, and B.-G. Park, Appl. Phys. Lett. **107**, 182407 (2015).

[59] R. J. Pedersen and F. L. Vernon, Appl. Phys. Lett. **10**, 29 (1967).

[60] J. S. Moodera, L. R. Kinder, J. Nowak, P. LeClair, and R. Meservey, Appl. Phys. Lett. **69**, 708 (1996).

[61] M. Johnson and R. H. Silsbee, Phys. Rev. B **37**, 5326 (1988).

[62] Z. M. Jin, A. Tkach, F. Casper, V. Spetter, H. Grimm, A. Thomas, T. Kampfrath, M. Bonn, M. Klaui, and D. Turchinovich, Nat. Phys. **11**, 761 (2015).

[63] M. H. Read and C. Altman, Appl. Phys. Lett. **7**, 51 (1965).

[64] L. A. Clevenger, A. Mutscheller, J. M. E. Harper, C. Cabral, and K. Barmak, J. Appl. Phys. **72**, 4918 (1992).

[65] A. Schauer, W. Peters, and W. Juergens, Thin Solid Films **8**, R9 (1971).

[66] N. Schwartz, W. A. Reed, P. Polash, and M. H. Read, Thin Solid Films **14**, 333 (1972).

[67] J. Narayan, V. Bhosle, A. Tiwari, A. Gupta, P. Kumar, and R. Wu, J. Vac. Sci. Technol. A **24**, 1948 (2006).

[68] K. Stella, D. Buerstel, S. Franzka, O. Posth, and D. Diesing, J. Phys. D: Appl. Phys. **42**, 135417 (2009).

[69] G. Y. Guo, Q. Niu, and N. Nagaosa, Phys. Rev. B **89**, 214406 (2014).

[70] J. Vogel, A. Fontaine, V. Cros, F. Petroff, J. P. Kappler, G. Krill, A. Rogalev, and J. Goulon, Phys. Rev. B **55**, 3663 (1997).

[71] F. Wilhelm, P. Poulopoulos, G. Ceballos, H. Wende, K. Baberschke, P. Srivastava, D. Benea, H. Ebert, M. Angelakeris, N. K. Flevaris, D. Niarchos, A. Rogalev, and N. B. Brookes, Phys. Rev. Lett. **85**, 413 (2000).

[72] W. Zhang, M. B. Jungfleisch, W. Jiang, Y. Liu, J. E. Pearson, S. G. E. te Velthuis, A. Hoffmann, F. Freimuth, and Y. Mokrousov, Phys. Rev. B **91**, 115316 (2015).

[73] W. F. Brinkman, R. C. Dynes, and J. M. Rowell, J. Appl. Phys. **41**, 1915 (1970).